Journal of Power Sources 196 (2011) 1561–1568

Contents lists available at ScienceDirect

Journal of Power Sources

journal homepage: www.elsevier.com/locate/jpowsour

Comparative study on the structure and electrochemical hydriding properties of MgTi, $Mg_{0.5}Ni_{0.5}Ti$ and $MgTi_{0.5}Ni_{0.5}$ alloys prepared by high energy ball milling

Steeve Rousselot, Daniel Guay, Lionel Roué*

INRS-Énergie, Matériaux et Télécommunications, 1650 Blvd. Lionel-Boulet, Varennes (Québec), Canada J3X 1S2

ARTICLE INFO

Article history:
Received 16 July 2010
Received in revised form 31 August 2010
Accepted 3 September 2010
Available online 15 September 2010

Keywords:
Mechanical alloying
Metal hydride
Mg–Ti–Ni based alloys
Ni–MH batteries

ABSTRACT

MgTi, $Mg_{0.5}Ni_{0.5}Ti$ and $MgTi_{0.5}Ni_{0.5}$ alloys doped with 10 wt.% Pd were prepared by high energy ball milling and evaluated as hydrogen storage electrodes for Ni–MH batteries. X-ray diffraction analyses indicated that the $Mg_{0.5}Ni_{0.5}Ti$ and $MgTi_{0.5}Ni_{0.5}$ alloys could be monophased or composed of a nanoscale mixture of MgTi + NiTi and MgTi + MgNi phases, respectively. Their hydrogen storage characteristics were investigated electrochemically in KOH electrolyte. No activation step was observed during the cycling of the Mg–Ti–Ni electrodes in contrast to that observed with the MgTi electrode. The highest hydrogen discharge capacity was obtained with the $MgTi_{0.5}Ni_{0.5}$ electrode (536 mAh g^{-1}) compared to 401 and 475 mAh g^{-1} for the $Mg_{0.5}Ni_{0.5}Ti$ and MgTi electrodes, respectively. The ternary Mg–Ti–Ni alloys showed a better cycle life with an average capacity decay rate per cycle lower than 1.5% compared to ~7% for the binary MgTi electrode. The Mg–Ni–Ti electrodes also displayed a much higher discharge rate capability than the binary MgTi electrode, especially with the $Mg_{0.5}Ni_{0.5}Ti$ electrode. The origin of this was established on the basis of the anodic polarization curves, where a substantial decrease of the concentration overpotential (reflecting a higher hydrogen diffusivity) was observed for the $Mg_{0.5}Ni_{0.5}Ti$ electrode.

1. Introduction

Several studies have recently shown that metastable Mg–Ti based alloys are promising metal hydride (MH) electrodes for Ni–MH batteries. The most remarkable performance was observed for Pd-capped Mg–Ti thin films prepared by electron beam deposition and magnetron co-sputtering with a reversible capacity of 1750 mAh g^{-1} for $Mg_{80}Ti_{20}$ [1] in comparison to only ~300 mAh g^{-1} for $LaNi_5$-based alloys used in commercial Ni–MH batteries. Their remarkable electrochemical H-storage properties was attributed to the face-centered-cubic (fcc) structure of the Mg–Ti–H phase, enabling much faster hydrogen diffusion than the rutile structure of pure MgH_2 [2]. However, their use in commercial Ni–MH batteries requires their synthesis in bulk form and large scale, which is challenging because the Mg–Ti system is almost immiscible under equilibrium conditions [3].

Several studies have demonstrated the possibility of producing bulk metastable Mg–Ti alloys in a large stoichiometry range and with various crystal structures by mechanical alloying [4–11]. For instance, we have shown that as-milled $Mg_{(100-x)}Ti_x$ ($40 \le x \le 80$) alloys comprise two phases, namely a Ti-rich hexagonal-close-packed (hcp) phase and a body-centered-cubic (bcc) phase [9]. Their proportion and stoichiometry vary with the nominal composition of the initial powder mixture. Upon electrochemical hydrogenation, both hcp and bcc phases are transformed into an fcc phase. $Mg_{50}Ti_{50}$ alloy has the highest hydrogen discharge capacity (475 mAh g^{-1}), which is comparable to that found by Kalisvaart et al. [5,6] for ball-milled Mg–Ti alloys. Note that Mg–Ti materials prepared by mechanical alloying must be activated for electrochemical hydrogen storage by adding of few at.% of Pd upon milling, which greatly facilitates the charge-transfer reaction and destabilizes the Mg–Ti hydride [11]. The fact that the maximum discharge capacities of ball-milled Mg–Ti alloys are much lower than those obtained on Mg–Ti thin films [1] is presently unclear. It may result from higher kinetic limitations due to longer diffusion path lengths in Mg–Ti powder electrodes and/or because only one phase in ball-milled Mg–Ti materials is electrochemically active as suggested by Kalisvaart et al. [5].

Furthermore, the cycle lifetimes of MgTi-based electrodes are insufficient. For example, the discharge capacity decay of a ball-milled $Mg_{50}Ti_{50}$–10 wt.% Pd electrode is over 80% after only 20 charge–discharge cycles [9]. It is assumed that the capacity degradation is associated with the irreversible oxidation of the alloy by the electrolyte (KOH) leading to the formation of $Mg(OH)_2$ and TiO_2 on the surface of the alloy particles. This consumes active material and must affect the charge-transfer at the alloy/electrolyte interface. Also, we have shown that the electrode degradation rate depends on the amount of hydrogen desorbed from the active material [9]. This tends to demonstrate that the volume expansion/contraction of the alloy upon charge/discharge, and thus the

* Corresponding author. Tel.: +1 450 929 8185; fax: +1 450 929 8102.
E-mail address: roue@emt.inrs.ca (L. Roué).

0378-7753/$ – see front matter © 2010 Elsevier B.V. All rights reserved.
doi:10.1016/j.jpowsour.2010.09.008

associated particle pulverization phenomenon accelerating the alloy oxidation, is largely responsible for the rapid capacity decay with cycling of the MgTi-based electrodes, as previously shown for MgNi electrodes [12].

A possible way to decrease the capacity loss of MgTi-based alloys is to adjust the alloy composition by partial substitution of Mg and/or Ti with appropriate element(s) in order to improve the alloy oxidation resistance in KOH electrolyte and/or to diminish the electrode pulverization by decreasing the alloy expansion coefficient related to hydrogen absorption. The partial substitution of Mg and/or Ti may also have a positive effect on the charge/discharge capacity and kinetics of the electrode by modifying the metal–hydrogen interaction (electronic effect), by modifying the hydrogen site size (geometric effect) and/or by the formation of additional phases (synergetic effect).

Among the possible substitution elements for improving the cycle life of MgTi-based electrodes, nickel appears as an interesting element due to its good corrosion resistance in alkaline media. Moreover, Kalisvaart and Notten have shown that the secondary TiNi phase present in ball-milled $(Mg_{0.75}Ti_{0.25})_{0.90}Ni_{0.10}$ acts as a rapid diffusion path for hydrogen, improving the discharge capacity and rate capability of the alloy [6]. Additionally, a hydrogenographic study on Mg-based thin films has shown that for the $Mg_yNi_{0.3}Ti_{0.7-y}$ ($0.55 < y < 0.65$) compositions, the hydrides are significantly destabilized with respect to both the Mg–Ti and Mg–Ni hydrides [13].

The present work provides new data about the influence of Ni on the electrode performance of MgTi-based hydrogen storage alloys prepared by high energy ball milling. In a preliminary study (unpublished results), the addition of Ni and partial substitution of Mg or Ti by Ni have been studied through the compared analysis of $MgTiNi_x$, $Mg_{1-x}Ni_xTi$ and $MgTi_{1-x}Ni_x$ (with x ranging from 0.05 to 0.5). The most significant improvements in terms of cycle life were observed for $MgTi_{0.5}Ni_{0.5}$ and $Mg_{0.5}Ni_{0.5}Ti$ electrodes and thus, the present study is focused on these two materials. Their structure and electrochemical hydrogen storage properties are studied in detail and compared to those observed with binary MgTi, NiTi and MgNi alloys.

2. Experimental

2.1. Material synthesis

Pure Mg (99.9%, chips, Norsk Hydro), Ti (99.5%, −325 mesh, Alfa Aesar) and Ni powders (99.9%, −325 mesh, Alfa Aesar) were used as starting materials. Samples were prepared according to the following stoichiometries: MgTi, $Mg_{0.5}Ni_{0.5}Ti$, $MgTi_{0.5}Ni_{0.5}$, NiTi and MgNi. 10 wt.% of Pd powder (99.9%, −325 mesh, Alfa Aesar) was added in the starting powder mixtures as a hydrogenation catalyst [11]. Ball milling was conducted in cylindrical stainless steel containers (55 ml) with three stainless steel balls (one 14 mm and two 11 mm diameter). The ball-to-powder mass ratio was 9:1 for all experiments. The container was sealed under an argon atmosphere and placed in a vibratory type mill (Spex 8000 M). The milling duration was fixed at 20 h, except for MgNi which was milled for 10 h (a longer milling time inducing its crystallization into $Mg_2Ni + MgNi_2$) [14]. The milling yields (defined as the ratio of the powder masses after and before milling) were higher than 70% in all experiments, indicating moderate cold welding between the powder particles and the milling tools.

2.2. Material characterization

The materials were characterized by X-ray diffraction (XRD) using a Bruker D8 diffractometer with Cu Kα radiation.

The specific surface area of the as-milled powders was measured by Kr adsorption (multipoint BET) using a Quantachrome Autosorb Automated Gas Sorption system.

Scanning electron microscopy (SEM) observations were made using a Jeol JSM-6300F microscope. The composition of the as-milled powders was determined by energy dispersive X-ray (EDX) analysis.

2.3. Electrochemical experiments

Electrochemical charge/discharge cycling tests were carried out on an Arbin BT2000 battery tester at room temperature in a 6 M KOH electrolyte using a three-electrode cell. The working electrode was made of a mixture of 100 mg of active material, 800 mg of graphite and 20 mg of carbon black. The counter electrode was a nickel wire and the reference electrode was an Hg/HgO electrode. Unless otherwise indicated, the working electrode was charged at a current density of $-200\ mA\ g^{-1}$ for 3 h and discharged at $20\ mA\ g^{-1}$ followed by a deeper discharge at $5\ mA\ g^{-1}$ up to −0.4 V vs. Hg/HgO. The discharge capacities are reported in $mAh\ g^{-1}$ of active material.

Electrochemical hydrogen pressure–composition isotherms (PCT) were performed at room temperature (23 °C) on an Arbin BT2000 from equilibrium potential measurements in the discharge step. Measurements were performed on electrodes in a fully charged state at their highest H-storage capacity. A discharge current of $5\ mA\ g^{-1}$ was applied for 1 or 2 h and the stabilized equilibrium potential was measured after an open circuit period of 2 h, i.e. a sufficiently long time to observe a stable voltage (potential drift < 0.1 mV min^{-1}). The hydrogen pressure values (P_{H_2}) were calculated from the measured equilibrium potentials (E_{eq}) according to the equation [15]:

$$E_{eq}(\text{V vs. Hg/HgO}) = E^0_{Hg/HgO} - \frac{RT}{nF}\ln\left(\frac{P_{H_2}}{P_0}\right) = -0.926 - 0.0293\ \log P_{H_2}\ (\text{atm}) \quad (1)$$

Linear polarization data were measured on a Voltalab40 (Radiometer Analytical) potentiostat/galvanostat/FRA apparatus. Prior to the linear polarization measurements, the electrode was fully charged at $-200\ mA\ g^{-1}$ for 3 h and remained in open circuit conditions for 2 h, up to stabilization of the open circuit potential. Anodic polarization curves were then obtained by scanning the electrode potential from 0 to 700 mV (vs. open circuit potential) at $1\ mV\ s^{-1}$. The curves were corrected for the ohmic drop determined from impedance measurements.

3. Results and discussion

3.1. Morphology and composition

Fig. 1 shows the SEM micrographs of milled MgTi (A), $Mg_{0.5}Ni_{0.5}Ti$ (B) and $MgTi_{0.5}Ni_{0.5}$ (C) powders. As seen in Fig. 1(C), the milled powders consist of irregular and porous agglomerates made up of many smaller particles (~1–10 μm) welded together, resulting from the repeated cold welding/fracturing processes occurring during ball milling. The mean size of the agglomerates is larger for the $Mg_{0.5}Ni_{0.5}Ti$ and $MgTi_{0.5}Ni_{0.5}$ powders (~50–200 μm) than that observed for the MgTi powder (~10–50 μm). This may reflect the increase of the ductility of the material with the addition of Ni, favoring powder cold welding upon milling. As a consequence, the specific surface area (S_{BET}) of the $Mg_{0.5}Ni_{0.5}Ti$ and $MgTi_{0.5}Ni_{0.5}$ powders is smaller than that of the MgTi powder (S_{BET} = 0.05, 0.07 and 0.19 $m^2\ g^{-1}$, respectively).

An EDX analysis of the milled powders show that all elements are homogeneously distributed and the composition of the as-

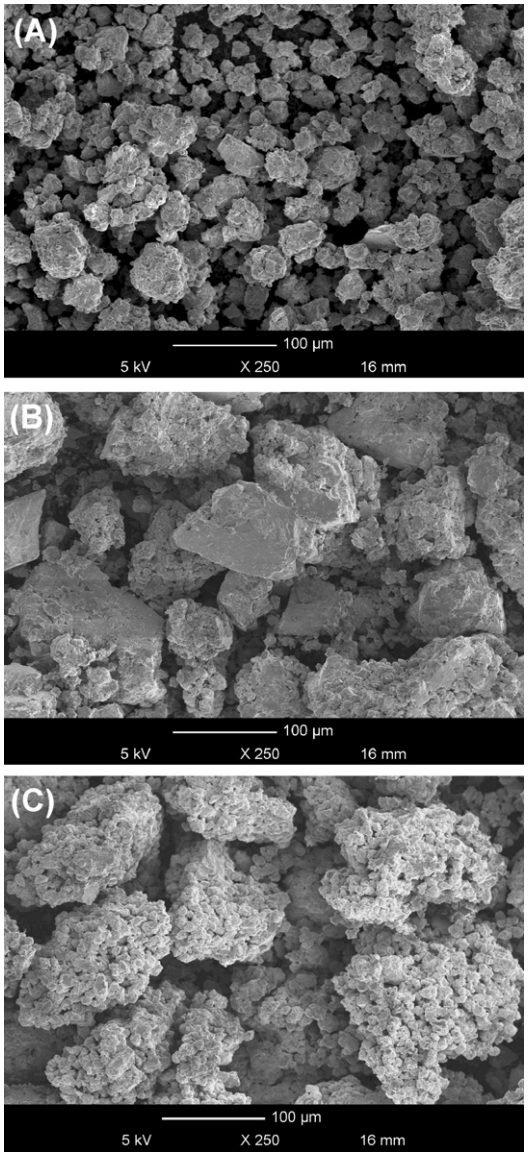

Fig. 1. SEM micrographs of 20 h-milled (A) MgTi, (B) $Mg_{0.5}Ni_{0.5}Ti$ and (C) $MgTi_{0.5}Ni_{0.5}$ powders.

milled powders does not differ by more than 2 at.% from their nominal composition, which indicates there is no preferential sticking to the balls and crucible wall upon milling. In addition, an iron contamination less than 1 at.% was measured, confirming the limited erosion of the container and balls.

3.2. Structure

Fig. 2 shows the XRD patterns of $MgTi_{0.5}Ni_{0.5}$, $Mg_{0.5}Ni_{0.5}Ti$ and MgTi. For comparison, the XRD patterns of NiTi and MgNi are also shown. All the XRD patterns display a broad peak located at ca. $2\theta = 40^\circ$. In some cases, small diffraction peaks are superimposed on this broad feature. They are associated with the presence of trace amounts of Ni ($2\theta = 45^\circ$), Mg ($2\theta = 35^\circ$) and possibly Ti ($2\theta = 41^\circ$). The XRD pattern of MgTi milled 20 h has already been analyzed in detail elsewhere [9] and it was shown that milling of Mg and Ti yields to the formation of a mixture of bcc (84 wt.%) and hcp (16 wt.%) phases. In the case of $Mg_{0.5}Ni_{0.5}Ti$ and $MgTi_{0.5}Ni_{0.5}$, the XRD patterns of the powder mixture were analyzed with respect to the milling time (not shown). After 5 h of milling, the diffraction peaks of Mg disappear from the XRD patterns while those of Ni are always present. Instead, in both cases, a broad diffraction peak is observed at ca. $2\theta = 38^\circ$, which is reminiscent of the same structure observed in the XRD pattern of MgTi (Fig. 2). This suggests that bcc MgTi is formed at the very beginning of the milling process in both cases. Upon further milling of $MgTi_{0.5}Ni_{0.5}$ and $Mg_{0.5}Ni_{0.5}Ti$, the diffraction peaks of Ti and Ni disappear and a new broad peak centered at ca. $2\theta = 42^\circ$ slowly grows. In the case of $MgTi_{0.5}Ni_{0.5}$, it is believed this peak is associated with the formation of TiNi, while it would reflect the presence of MgNi in the case of $MgTi_{0.5}Ni_{0.5}$.

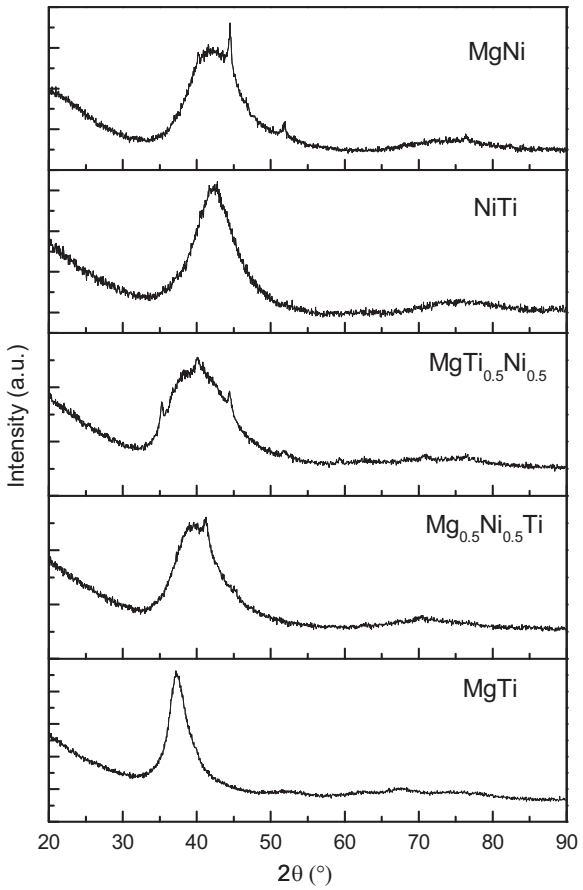

Fig. 2. XRD patterns of milled MgTi, $Mg_{0.5}Ni_{0.5}Ti$, $MgTi_{0.5}Ni_{0.5}$, NiTi and MgNi powders.

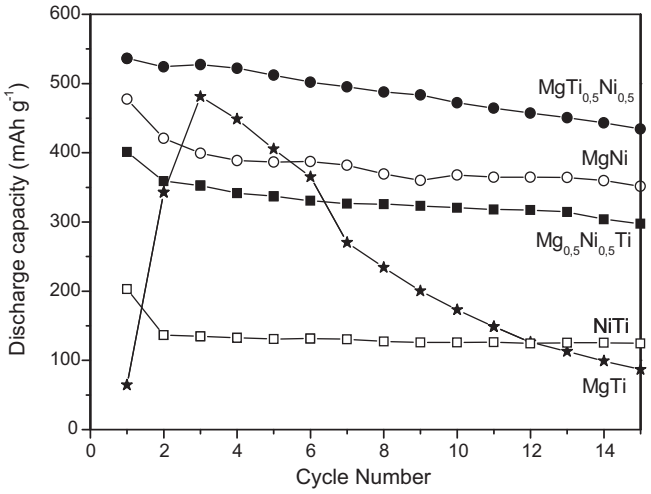

Fig. 3. Evolution with cycling of the discharge capacities of the MgTi, $Mg_{0.5}Ni_{0.5}Ti$, $MgTi_{0.5}Ni_{0.5}$, NiTi and MgNi electrodes.

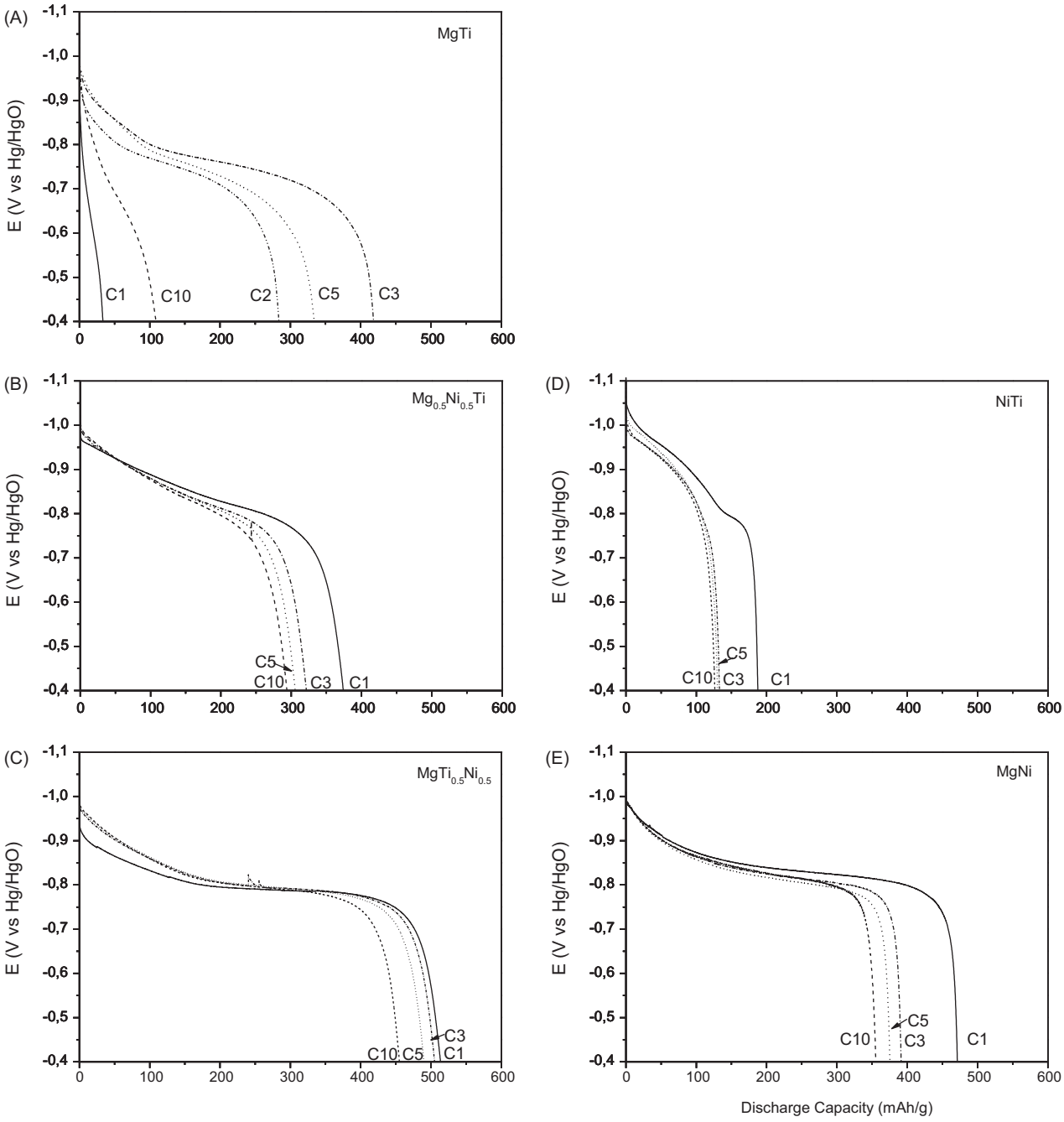

Fig. 4. Evolution of the discharge curves with cycling of the (A) MgTi, (B) $Mg_{0.5}Ni_{0.5}Ti$, (C) $MgTi_{0.5}Ni_{0.5}$, (D) NiTi and (E) MgNi electrodes.

Accordingly, $MgTi_{0.5}Ni_{0.5}$ would be composed of MgTi and MgNi, while $Mg_{0.5}Ni_{0.5}Ti$ would be composed of MgTi and TiNi. However, considering the breadth of the diffraction peaks after 20 h of milling, one cannot exclude the possibility that the $MgTi_{0.5}Ni_{0.5}$ and $Mg_{0.5}Ni_{0.5}Ti$ materials are monophased. In the future, transmission electron microscopy with electron diffraction analyses should be done to resolve this issue.

3.3. Electrochemical hydriding properties

3.3.1. Cycling discharge capacity

The evolution of the discharge capacities with cycling of the MgTi, $Mg_{0.5}Ni_{0.5}Ti$ and $MgTi_{0.5}Ni_{0.5}$ electrodes is shown in Fig. 3. For comparison, the cycling discharge capacities of NiTi and MgNi are also shown. The $Mg_{0.5}Ni_{0.5}Ti$ and $MgTi_{0.5}Ni_{0.5}$ electrodes exhibit a similar behavior, i.e. their discharge capacity is highest during the first cycle and then decreases slowly with cycling. In contrast, the MgTi electrode needs three activation cycles before reaching its maximum discharge capacity, and then it decreases rapidly with cycling. It was shown in a previous study that the activation period observed upon charge/discharge cycling on MgTi alloy is related to a structural transition from a bcc/hcp phase mixture to a fcc phase that occurs during the first few cycles [9]. The absence of an activation period on the $Mg_{0.5}Ni_{0.5}Ti$ and $MgTi_{0.5}Ni_{0.5}$ electrodes may indicate that such a phase transition does not occur with these materials. This tends to demonstrate that these two compounds are monophased, i.e. they do not contain secondary MgTi phase. However, the presence a significant proportion of MgTi phase in the $Mg_{0.5}Ni_{0.5}Ti$ and $MgTi_{0.5}Ni_{0.5}$ compounds cannot be totally excluded if we assume that the presence of the MgNi or NiTi

phase in the ternary Mg–Ti–Ni compounds accelerates the hydrogenation of the MgTi phase and thus the activation period could be eliminated (at least, on the time scale of the present charge period). Note that our work on $Mg_{1-x}Ni_xTi$ and $MgTi_{1-x}Ni_x$ with x ranging from 0.05 to 0.5 (not shown) indicates a progressive decrease of the number of activation cycles as x increases (i.e, the maximum discharge capacity was reached at the 3rd cycle for $x = 0$ and 0.05, at the 2nd cycle for $x = 0.1$ and 0.3 and at the 1st cycle for $x = 0.5$).

The maximum discharge capacities of the $Mg_{0.5}Ni_{0.5}Ti$, $MgTi_{0.5}Ni_{0.5}$ and MgTi electrodes are 401, 536 and 475 mAh g^{-1}, respectively (Fig. 3). The lower electrochemical H-storage capacity of $Mg_{0.5}Ni_{0.5}Ti$ is not surprising considering the smaller amount of Mg. In comparison, the maximum discharge capacities of the NiTi and MgNi electrodes are 202 and 478 mAh g^{-1}, respectively (Fig. 3).

In addition, as seen in Fig. 3, the capacity decay with cycling is much less pronounced for the $Mg_{0.5}Ni_{0.5}Ti$ and $MgTi_{0.5}Ni_{0.5}$ electrodes than for the MgTi electrode. Indeed, the average capacity decay (measured between the 3rd and the 15th cycle) for the $Mg_{0.5}Ni_{0.5}Ti$ and $MgTi_{0.5}Ni_{0.5}$ electrodes is respectively ca. 5 and 8 mAh g^{-1} (or 1.3 and 1.45%) per cycle compared to 30 mAh g^{-1} (6.7%) per cycle for the MgTi electrode. Considering that the capacity degradation with cycling of the MgTi electrode is due to its irreversible oxidation ($Mg(OH)_2$ and TiO_2 formation) by the KOH electrolyte which is largely accentuated by its decrepitation [9], these results illustrate the very positive effect of the partial substitution of Mg or Ti by Ni on the oxidation and/or pulverization resistance of the active material. The lower specific surface area (i.e., larger particle size as seen in Fig. 1) of $Mg_{0.5}Ni_{0.5}Ti$ and $MgTi_{0.5}Ni_{0.5}$ compared to MgTi could also induce a decrease of their oxidation rate upon cycling as demonstrated on MgNi electrodes made of large (>150 μm) particles [16]. The cracking of the Mg–Ni–Ti particles upon cycling may also be less extensive due to their higher ductility.

Fig. 4 shows the evolution with cycling of the discharge curves on MgTi (A), $Mg_{0.5}Ni_{0.5}Ti$ (B) and $MgTi_{0.5}Ni_{0.5}$ (C) electrodes. For comparison, the discharge curves of NiTi (D) and MgNi (E) electrodes are also shown. For these experiments, the electrodes were charged at −200 mA g^{-1} for 3 h and discharged at 20 mA g^{-1} up to −0.4 V vs. Hg/HgO. As seen in Fig. 4(A), the shape of the discharge curve of the MgTi electrode is notably modified during the first three cycles. This behavior is associated with the irreversible phase transition that occurs during the activation period as discussed previously. At the third cycle, a well-defined voltage plateau related to the H-desorption reaction (β-to-α phase transition) is observed at about −0.75 V. The progressive potential shift and shortening of the H-desorption plateau during the subsequent cycles reflects the major increase of the electrode polarization resistance and consumption of the active material due to its irreversible oxidation and cracking. For the $Mg_{0.5}Ni_{0.5}Ti$ electrode (Fig. 4(B)), a "sloping H-desorption plateau" centered around −0.85 V appears from the first cycle. Its shortening and potential shift upon cycling is much less pronounced than that observed for the MgTi electrode (Fig. 4(A)), reflecting its much lower degradation rate. For the $MgTi_{0.5}Ni_{0.5}$ electrode (Fig. 4(C)), a well-defined discharge plateau centered at about −0.8 V is observed. Its voltage position does not change with cycling, indicating that the electrode polarization resistance does not increase significantly upon cycling. No evident discontinuity characteristic of a multiphase system appears in the discharge curves of $Mg_{0.5}Ni_{0.5}Ti$ and $MgTi_{0.5}Ni_{0.5}$ electrodes. This tends to indicate that these two materials are monophased. However, the hypothesis of a multiphase system cannot be rejected on the basis of these observations because a broadening of the energy spectrum of each type of H occupation site may occur in ball-milled multiphase materials resulting in the disappearance of the discontinuities of the discharge curves. Moreover, the discharge

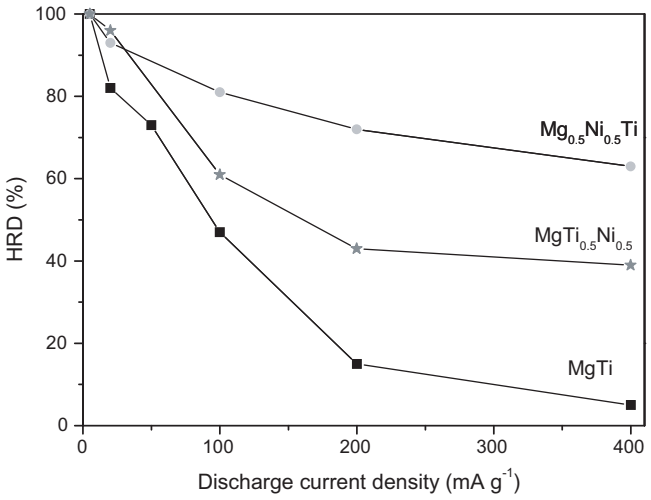

Fig. 5. High-rate dischargeability with respect to the discharge current of the MgTi, $Mg_{0.5}Ni_{0.5}Ti$ and $MgTi_{0.5}Ni_{0.5}$ electrodes.

potential regions of the NiTi (Fig. 4(D)) and MgNi (Fig. 4(E)) electrodes are very close to that of the MgTi electrode, which makes their differentiation difficult. Additionally, the fact that the plateau discharge potentials for the $Mg_{0.5}Ni_{0.5}Ti$ electrode (ca. −0.85 V) and the $MgTi_{0.5}Ni_{0.5}$ electrode (ca. −0.80 V) are more negative than that for the MgTi electrode (ca. −0.75 V at the 3rd cycle) indicates that the H-desorption reaction is facilitated for the ternary Mg–Ti–Ni electrodes as confirmed below.

3.3.2. High-rate dischargeability

Fig. 5 shows the discharge efficiency or high-rate dischargeability (HRD) of the MgTi, $Mg_{0.5}Ni_{0.5}Ti$ and $MgTi_{0.5}Ni_{0.5}$ electrodes, depending on the discharge current. The HRD is defined and calculated according to the formula:

$$\text{HRD}\ (\%) = \frac{C^x}{C^x + C^5} \times 100 \quad (2)$$

where C^x is the maximum discharge capacity obtained at the discharge current density of x mA g^{-1} and C^5 is the residual discharge capacity extracted at a discharge current density of 5 mA g^{-1} after the electrode is discharged at x mA g^{-1}. The cut-off discharge potential was fixed at −0.4 V vs. Hg/HgO. As shown in Fig. 5, the HRD of the ternary Mg–Ni–Ti alloys are higher than that of the binary MgTi alloy. This is more remarkable with the $Mg_{0.5}Ni_{0.5}Ti$ electrode, which displays, at a discharge current density of 400 mA g^{-1}, a HRD value of 63% compared to 39 and 5% for the $MgTi_{0.5}Ni_{0.5}$ and MgTi electrodes, respectively.

The increase of the HRD for the ternary Mg–Ni–Ti alloys can result from a decrease of the hydride stability and/or an improvement of the charge-transfer reaction (inducing a decrease of the activation overpotential) or else from an increase of the hydrogen diffusivity (inducing a decrease of the concentration overpotential). These different components are determined and compared for the MgTi, $Mg_{0.5}Ni_{0.5}Ti$ and $MgTi_{0.5}Ni_{0.5}$ materials in the following sections.

3.3.3. Electrochemical pressure–composition isotherms

Fig. 6 shows the electrochemical pressure–composition isotherms (PCT) for the MgTi, $Mg_{0.5}Ni_{0.5}Ti$ and $MgTi_{0.5}Ni_{0.5}$ electrodes. They are expressed as a function of the depth of charge of the electrode rather than as a function of the H content in order to facilitate the comparison between the different curves. A rather well-defined H-desorption plateau ($\alpha + \beta$ mixed region) is observed for the MgTi and $MgTi_{0.5}Ni_{0.5}$ electrodes while no

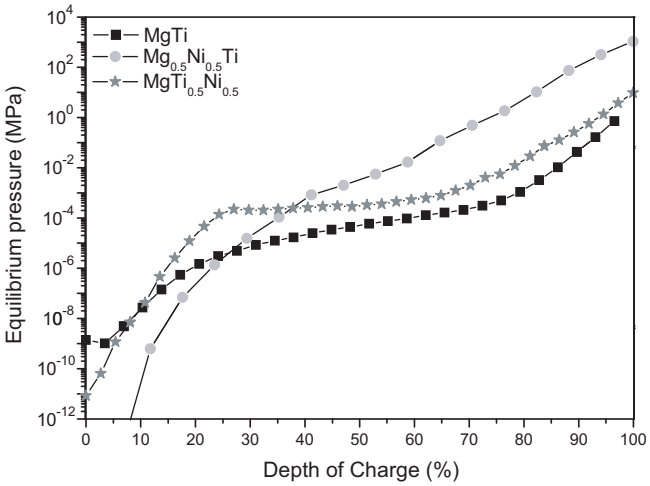

Fig. 6. Electrochemical hydrogen pressure–composition isotherms (discharged at room temperature) of the MgTi, $Mg_{0.5}Ni_{0.5}Ti$ and $MgTi_{0.5}Ni_{0.5}$ alloys.

Table 1
Electrochemical kinetic parameters of the MgTi, $Mg_{0.5}Ni_{0.5}Ti$ and $MgTi_{0.5}Ni_{0.5}$ electrodes.

Alloy	i_L (mA g^{-1})	i_0 (mA g^{-1})	α
MgTi	270	53	0.72
$MgTi_{0.5}Ni_{0.5}$	689	140	0.72
$Mg_{0.5}Ni_{0.5}Ti$	1131	167	0.74

plateau is discernible for the $Mg_{0.5}Ni_{0.5}Ti$ electrode. The absence of a plateau region for the latter is in accordance with the discharge curve shape shown in Fig. 4(B) and confirms the larger distribution of energy levels for hydrogen in this material.

In addition, an increase of the equilibrium hydrogen pressure is observed with the Mg–Ti–Ni alloys. For example, at a depth of charge of 50%, an equilibrium hydrogen pressure of ca. 5×10^{-5}, 3×10^{-4} and 4×10^{-3} MPa is measured for MgTi, $MgTi_{0.5}Ni_{0.5}$ and $Mg_{0.5}Ni_{0.5}Ti$, respectively. This indicates that the Mg–Ti–Ni hydrides are destabilized with respect to the Mg–Ti hydride. This destabilization must positively affect their high-rate dischargeability by decreasing the electrode equilibrium potential and mostly by decreasing the hydrogen diffusion resistance (as confirmed below).

3.3.4. Anodic polarization curves

Fig. 7(A) shows the anodic polarization curves on fully charged MgTi, $Mg_{0.5}Ni_{0.5}Ti$ and $MgTi_{0.5}Ni_{0.5}$ electrodes. These curves were measured when the electrodes reached their highest capacity, i.e. at the 3rd cycle for MgTi and the 1st cycle for $Mg_{0.5}Ni_{0.5}Ti$ and $MgTi_{0.5}Ni_{0.5}$. The anodic current (i) increases as the overpotential (η) increases, reaching a limiting current (i_L) that results from a mass transport limitation of the hydrogen atoms in the alloy. The i_L values are listed in Table 1. The highest i_L value is obtained with the $Mg_{0.5}Ni_{0.5}Ti$ alloy (i_L = 1131 mA g^{-1}), confirming its better H-diffusion kinetic properties compared to those of $MgTi_{0.5}Ni_{0.5}$ (i_L = 689 mA g^{-1}) and, to a much larger extent, of MgTi (i_L = 270 mA g^{-1}).

The anodic overpotential, η, can be expressed as [17]

$$\eta = \frac{RT}{(1-\alpha)F} \ln\left(\frac{i}{i_0}\right) + \frac{RT}{(1-\alpha)F} \ln\left(\frac{i_L}{i_L - i}\right) \quad (3)$$

where R is the gas constant, F is the Faraday constant, T is the temperature, α is the charge-transfer coefficient and i_0 is the exchange current density. The first term on the right-hand side of Eq. (3) is the activation overpotential, η_a, due to the charge-transfer resistance and the second term is the concentration overpotential, η_c,

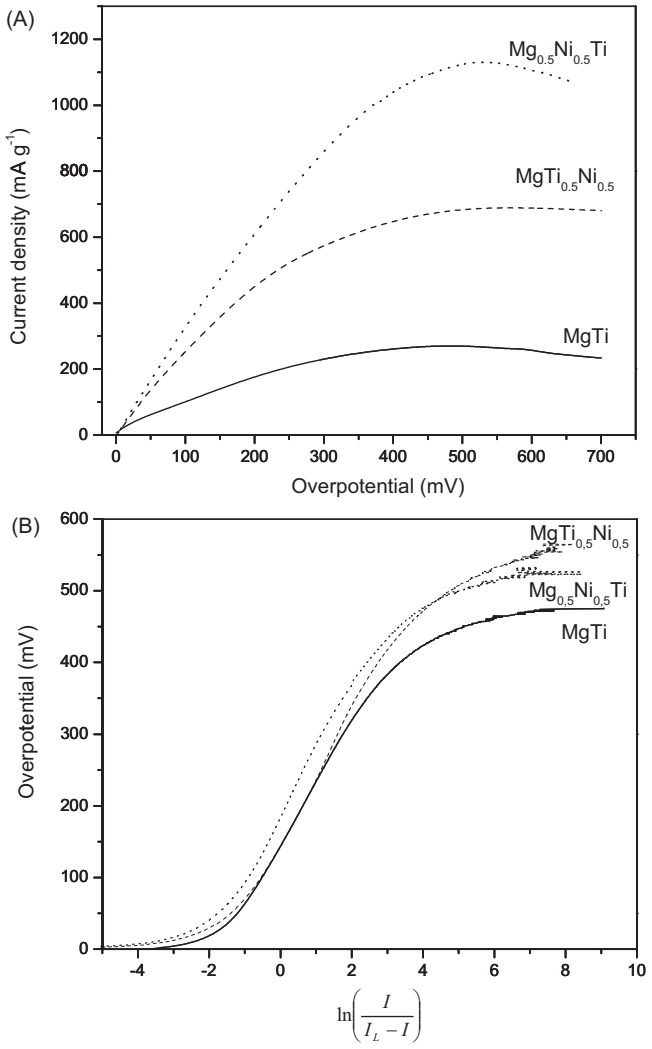

Fig. 7. (A) Anodic polarization curves for fully charged MgTi, $Mg_{0.5}Ni_{0.5}Ti$ and $MgTi_{0.5}Ni_{0.5}$ electrodes. Scan rate: 1 mV s^{-1}. (B) Overpotential as a function of $\ln[i/(i_L - i)]$ for the fully charged MgTi, $Mg_{0.5}Ni_{0.5}Ti$ and $MgTi_{0.5}Ni_{0.5}$ electrodes.

due to the H-diffusion resistance [18]. Rearranging Eq. (3) leads to the following expression [17]:

$$\eta = \frac{RT}{(1-\alpha)F} \ln\left(\frac{i_L}{i_0}\right) + \frac{RT}{(1-\alpha)F} \ln\left(\frac{i}{i_L - i}\right) \quad (4)$$

According to Eq. (4), a plot of η vs. $\ln[i/(i_L - i)]$ produces a straight line in the middle range of overpotential as shown in Fig. 7(B), permitting the determination of the α and i_0 values from the slope and intercept, respectively [18]. These values are listed in Table 1. The exchange current density is much higher for $Mg_{0.5}Ni_{0.5}Ti$ (i_0 = 167 mA g^{-1}) and $MgTi_{0.5}Ni_{0.5}$ (i_0 = 140 mA g^{-1}) than for MgTi (i_0 = 53 mA g^{-1}), despite the fact than the specific surface areas of the as-milled Mg–Ni–Ti powders are about 3 times lower than that of the MgTi powder as shown previously. This illustrates the very positive effect of Ni on the kinetics of the charge-transfer reaction on the alloy surface. In comparison, the i_0 values compiled by Feng et al. [19] are ~20–300 mA g^{-1} on $LaNi_5$-based and ~20–100 mA g^{-1} on Zr-based materials (after activation and at fully charged state). On the other hand, as seen in Table 1, the charge-transfer coefficient is similar for the three alloys ($\alpha \sim 0.7$).

In order to differentiate the contribution of the charge-transfer resistance and H-diffusion resistance to the anodic polarization, Eq. (3) was used to calculate the value of the activation overpotential (η_a) and the concentration overpotential (η_c). Their evolution as a

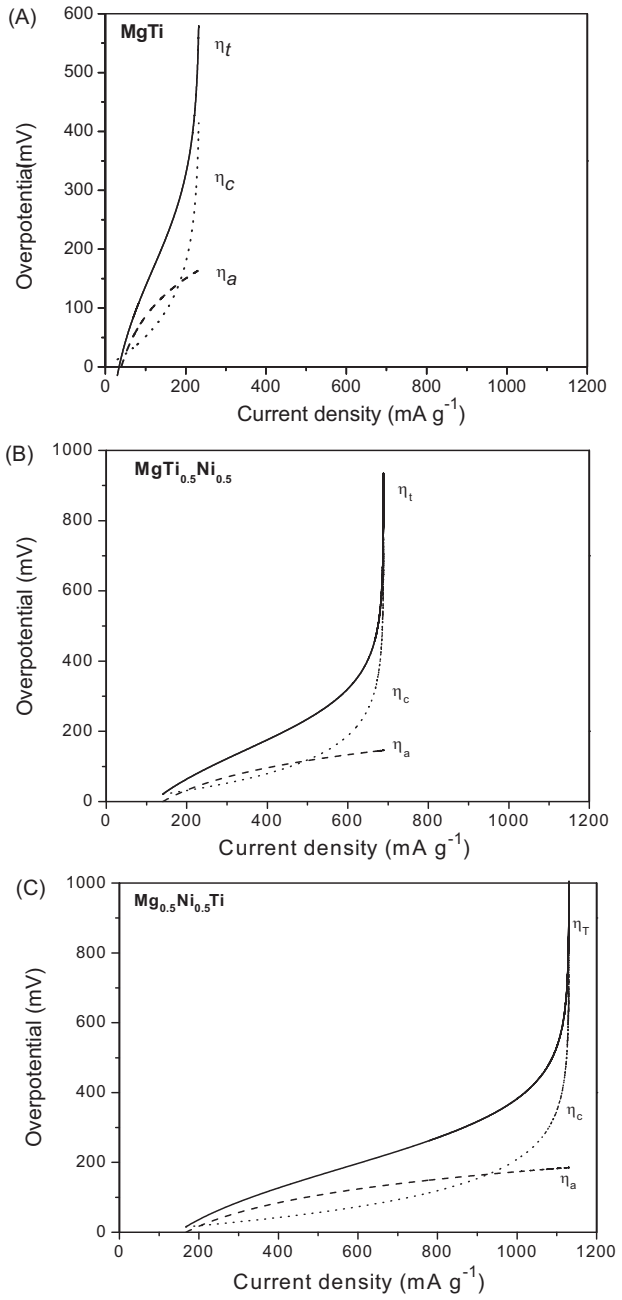

Fig. 8. Evolution of the total overpotential (η_t), activation overpotential (η_a) and concentration overpotential (η_c) as a function of the discharge current for the (A) MgTi, (B) $MgTi_{0.5}Ni_{0.5}$ and (C) $Mg_{0.5}Ni_{0.5}Ti$ electrodes (in a fully charged state).

function of the discharge current is shown in Fig. 8 for the MgTi (A), $MgTi_{0.5}Ni_{0.5}$ (B) and $Mg_{0.5}Ni_{0.5}Ti$ (C) electrodes. As expected, η_a is higher than η_c at lower discharge current densities and η_c becomes largely dominant at higher discharge current densities for all electrodes. Similar behavior was observed on AB_2-type [18] and AB_5-type [20,21] hydrogen storage alloys. However, as seen in Fig. 8, both η_a and η_c contributions are significant over a large range of discharge current density, meaning that the discharge process is under mixed control in this region. Actually, based on our previous study on the MgTi electrode [11], it is assumed that the charge-transfer reaction is the rate-determining step only when the applied discharge current density is lower than the exchange current density (Table 1), i.e. for a discharge current value lower than 53, 140 and 167 mA g^{-1} for MgTi, $MgTi_{0.5}Ni_{0.5}$ and $Mg_{0.5}Ni_{0.5}Ti$, respectively. On the other hand, the electrode reaction is assumed to be mainly controlled by the H-diffusion process in the bulk alloy when η_c exceeds η_a (Fig. 8), i.e. at a critical discharge current density of 173, 494 and 934 mA g^{-1} for MgTi, $MgTi_{0.5}Ni_{0.5}$ and $Mg_{0.5}Ni_{0.5}Ti$, respectively. A comparison of Fig. 8(A)–(C) clearly shows that the $Mg_{0.5}Ni_{0.5}Ti$ electrode has the smallest overpotential followed by $MgTi_{0.5}Ni_{0.5}$ and, far behind, MgTi. This is consistent with their HRD performance shown in Fig. 5.

4. Conclusions

The influence of Ni on the structure and electrochemical H-storage properties of MgTi-based electrodes have been studied through the comparative analysis of ball-milled MgTi, $Mg_{0.5}Ni_{0.5}Ti$ and $MgTi_{0.5}Ni_{0.5}$ materials doped with 10 wt.% Pd. The main results are summarized as follows:

1. On the basis of the XRD patterns, the $MgTi_{0.5}Ni_{0.5}$ and $Mg_{0.5}Ni_{0.5}Ti$ alloys may be composed of a mixture of MgTi + MgNi and MgTi + NiTi phases, respectively, or made of a single phase that contains all the elements. The resolution of this issue will await detailed TEM analyses.
2. In contrast to that observed on the binary MgTi alloy, no activation period was observed upon charge–discharge cycling on the ternary Mg–Ti–Ni alloys.
3. The $MgTi_{0.5}Ni_{0.5}$ electrode showed the highest discharge capacity (536 mAh g^{-1}) compared to 401 and 475 mAh g^{-1} for the $Mg_{0.5}Ni_{0.5}Ti$ and MgTi electrodes, respectively.
4. The ternary Mg–Ti–Ni electrodes displayed a much better cycle life than the MgTi electrode, with an average capacity decay rate per cycle <1.5% compared to ~7% for the binary MgTi electrode.
5. The ternary Mg–Ni–Ti electrodes had a much higher discharge rate capability than the binary MgTi electrode. This was more remarkable for the $Mg_{0.5}Ni_{0.5}Ti$ electrode (HRD of 63% at a discharge current density of 400 mA g^{-1} compared to 39 and 5% for the $MgTi_{0.5}Ni_{0.5}$ and MgTi electrodes, respectively).
6. The higher rate dischargeability of the $Mg_{0.5}Ni_{0.5}Ti$ electrode was mainly attributed to its better H-diffusion kinetic properties as illustrated by its low concentration overpotential compared to that of $MgTi_{0.5}Ni_{0.5}$ and, to a much larger extent, to that of MgTi.

Acknowledgements

This work was financially supported by the Natural Sciences and Engineering Research Council (NSERC) and the "Fonds Québecois de la Recherche sur la Nature et les Technologies" (FQRNT).

References

[1] P. Vermeulen, R.A.H. Niessen, D.M. Borsa, B. Dam, R. Grissen, P.H.L. Notten, Electrochem. Solid-State Lett. 9 (2005) A520.
[2] P. Vermeulen, H.J. Wondergem, P.C.J. Graat, D.M. Borsa, H. Schreuders, B. Dam, R. Griessen, P.H.L. Notten, J. Mater. Chem. 18 (2008) 3680.
[3] A.A. Nayeb-Hashemi, J.B. Clark, Phase Diagrams of Binary Magnesium Alloys, ASM International, Metals Park, OH, 1998.
[4] M. Hida, K. Asai, Y. Takemoto, A. Sakakibara, Mater. Trans. 37 (1996) 1679.
[5] W.P. Kalisvaart, H.J. Wondergem, F. Bakker, P.H.L. Notten, J. Mater. Res. 22 (2007) 1640.
[6] W.P. Kalisvaart, P.H.L. Notten, J. Mater. Res. 23 (2008) 2179.
[7] K. Asano, H. Enoki, E. Akiba, J. Alloys Compd. 480 (2009) 558.
[8] S. Rousselot, M.P. Bichat, D. Guay, L. Roué, J. Power Sources 175 (2008) 621.
[9] S. Rousselot, M.P. Bichat, D. Guay, L. Roué, J. Electrochem. Soc. 156 (2009) A967.
[10] S. Rousselot, D. Guay, L. Roué, J. Power Sources 195 (2010) 4370.
[11] S. Rousselot, D. Guay, L. Roué, Electrochim. Acta 55 (2010) 611.
[12] S. Ruggeri, L. Roué, J. Power Sources 117 (2003) 260.
[13] R. Gremaud, C.P. Broedersz, D.M. Borsa, A. Borgschulte, P. Mauron, H. Schreuders, J.H. Rector, B. Dam, R. Griessen, Adv. Mater. 19 (2007) 2813.
[14] S. Ruggeri, C. Lenain, L. Roué, G. Liang, J. Huot, R. Schulz, J. Alloys Compd. 339 (2002) 195.
[15] A. Züttel, V. Güther, A. Otto, M. Bärtsch, R. Kötz, D. Chartouni, Ch. Nüttzenadel, L. Schlapbach, J. Alloys Compd. 293–295 (1999) 663.

[16] C. Rongeat, L. Roué, J. Power Sources 132 (2004) 302.
[17] A.J. Bard, L.R. Faulkner, Electrochemical Methods—Fundamentals and Applications, 2nd ed., John Wiley & Sons Inc., New York, 2001.
[18] H.W. Yang, Y.Y. Wang, C.C. Wan, J. Electrochem. Soc. 143 (1996) 429.
[19] F. Feng, M. Geng, D.O. Northwood, Int. J. Hydrogen Energy 26 (2001) 725.
[20] X. Yuan, N. Xu, J. Electrochem. Soc. 149 (2002) A407.
[21] M.S. Wu, H.R. Wu, Y.Y. Wang, C.C. Wan, J. Appl. Electrochem. 33 (2003) 619.